Thermal Science and Engineering Progress 60 (2025) 103418

Contents lists available at ScienceDirect

Thermal Science and Engineering Progress

journal homepage: www.elsevier.com/locate/tsep

Influence of thermal contrast and limitations of a deep-learning based estimation of early-stage tumour parameters in different breast shapes using simulated passive and dynamic thermography

M.F.B. Moraes [a], S. Sfarra [c], H. Fernandes [d,e,*], A.A.A. Figueiredo [a,b]

[a] Post-Graduate Program in Mechanical Engineering, Federal Institute of Maranhão, São Luis, Brazil
[b] Department of Mechanical Engineering, State University of Maranhão, São Luis, Brazil
[c] Department of Industrial and Information Engineering and Economics, University of L'Aquila, L'Aquila, Italy
[d] IVHM Centre, School of Aerospace, Transport and Manufacturing, Cranfield University, Cranfield, United Kingdom
[e] Faculty of Computing, Federal University of Uberlandia, Uberlandia, Brazil

ARTICLE INFO

Keywords:
Bio-heat transfer
Breast tumour
Dynamic thermography
Inverse problem
Neural network

ABSTRACT

To enhance diagnostic sensitivity compared to passive thermography, thermal stress can be applied to the breast surface with the temperatures being measured in the thermal recovery phase, a process called dynamic thermography. This study aims to evaluate the limitations of both passive and dynamic thermography in estimating early-stage tumour parameters across different breast shapes and how to improve the results. Three breast models with thermoregulation were solved numerically using COMSOL Multiphysics®. A neural network developed in PyTorch was used to estimate breast tumour location and size. The estimates obtained using each approach were compared, and the effects of thermal contrast, noise, and tumour depth range were analysed. Dynamic thermography provided the most accurate estimates compared to passive thermography, with mean error reductions that reached up to 33.25%. Additionally, the number of estimates with errors higher than 10% was up to 48.42% lower. Tumour radius showed the lowest noise threshold, providing the highest estimations errors. Adding deeper tumours to the datasets caused mean error increases of up to 51.27%. Thus, this work contributes by comparing both types of thermography, analysing thermal aspects of the temperature data that influences the neural network's estimation process, and suggesting alternatives to improve its accuracy.

1. Introduction

Breast cancer is the most commonly diagnosed and leading cause of cancer-related death among women worldwide, accounting for 23.76% of all cancer diagnoses and 15.44% of cancer-related fatalities in 2022 [1]. Various screening methods, such as mammography, magnetic resonance imaging (MRI) and ultrasound have been used in breast cancer detection, with an early diagnosis reducing a patient's mortality rate and annual cost of treatment [2,3].

Mammography is the gold standard of breast cancer imaging techniques, having benefits such as high sensitivity and specificity [4]. However, this method has limitations, for instance, the emission of ionizing radiation, the discomfort of compression and low effectiveness for dense and surgically implanted breasts [5,6]. Infrared thermography is a non-invasive and cost-effective screening method that can complement mammography [7,8]. Malignant tumours generate significant heat due to their high metabolic rates and the formation of new blood vessels (angiogenesis). The heat can reach the breast's surface, forming temperature maps that can be observed using an infrared camera [9,10].

Two types of thermography can be used for medical screening and diagnosis: passive thermography, where the temperatures are measured when the patient is acclimatised in a temperature-controlled environment; and dynamic thermography, where heating stress (hyperthermia) or cooling stress (hypothermia) is applied on the tissue, with the temperatures being measured during thermal recovery [11–14]. The thermal stress used in dynamic thermography enhances thermal contrast, the temperature difference between cancerous and healthy tissue, which improves the sensitivity and effectiveness of tumour imaging [15–17].

Many researchers have used neural networks to estimate breast tumour parameters based on passive and dynamic infrared imaging. Medical practitioners can use the estimated parameters to define the most appropriate cancer treatment [18]. In this approach, surface temperature measurements are used to train a neural network, so

* Corresponding author at: IVHM Centre, School of Aerospace, Transport and Manufacturing, Cranfield University, Cranfield, United Kingdom.
E-mail address: h.fernandes@cranfield.ac.uk (H. Fernandes).

https://doi.org/10.1016/j.tsep.2025.103418
Received 27 October 2024; Received in revised form 19 December 2024; Accepted 17 February 2025
Available online 24 February 2025
2451-9049/© 2025 The Authors. Published by Elsevier Ltd. This is an open access article under the CC BY-NC license (http://creativecommons.org/licenses/by-nc/4.0/).

the desired thermophysical and geometric tumour parameters can be estimated only with temperature data. Mitra and Balaji [19] used an artificial neural network and simulated surface temperature measurements to estimate breast tumours size and location, showing, respectively, relative errors of 10% and 22% with a 0.5 K noise. Saniei et al. [20] trained a neural network with simulated temperature profiles and estimated breast tumour depth and size using thermal images of histologically confirmed breast cancer patients. Deep-seated tumours had the largest estimation errors of all cases.

Majdoubi et al. [21] employed a feedforward neural network to estimate the location and the radius of breast cancer tumours using surface temperature distributions and isothermal contour plots. Tumours smaller than 0.5 cm presented larger errors when estimating their location and radius, especially in large-sized breasts. Chen et al. [22] combined a convolutional neural network and an autoencoder to estimate various parameters using simulated surface temperature data obtained under dynamic thermography conditions, with the estimated parameters showing relative errors lower than 1.2% when the temperatures had a noise level of 2%, except the blood perfusion rate, which showed a relative error of 18.75%. Khomsi et al. [23] employed a convolutional neural network to estimate the size and location of breast tumours using simulated surface temperature data. With a 0.1 noise, tumour depth had the largest estimation errors, showing a correlation coefficient of 0.78 and a mean squared error of 2.681.

All these studies investigated the isolated results of training a neural network with passive or dynamic thermography surface temperature data without analysing the advantages or disadvantages of one approach over the other. This is especially important when diagnosing small and deep-seated tumours, with lower thermal signatures that sometimes cannot be properly perceived using passive thermography. The collective and individual influence of thermal contrast in the parameter's estimation error and the consistency of the neural network's estimates have also not been investigated. This paper's primary focus is to provide information on the limits of using surface temperature data from passive and dynamic thermography to estimate early-stage breast tumours position and size, and ways of improving the estimates.

In this work, a feedforward neural network is developed using PyTorch to estimate the size and location of breast tumours based on simulated surface temperature measurements of breast models with different shapes under both passive and dynamic thermography conditions. Three breast models were solved numerically by COMSOL Multiphysics® to generate various surface temperature datasets. Thermoregulation effects attributed to the applied cold stress were modelled as temperature-dependent metabolic heat generation and blood perfusion rate. The neural network was trained multiple times to check its estimation consistency. Measurement errors were added to the simulated data as random noise. The results for two different depth ranges were investigated using both types of thermography. The influence of thermal contrast on the estimated parameters was also analysed.

This paper is arranged as follows: Section 2 presents the numerical breast model, governing equations, thermoregulation model, thermophysical properties of the tissue layers, and boundary conditions. The dataset generation algorithm, tumour depth ranges, and neural network structure are also shown. Section 3 shows the estimation errors in each depth range, and the effect of noise and thermal contrast on the estimates. Section 4 presents the concluding remarks.

2. Materials and methods

2.1. Mathematical model

Patients can have different breast shapes and sizes due to factors such as genetics, hormones, and age [24]. Because of this, the studied cases can also have different surface temperatures and thermal responses. Considering this phenomenon, three breast models were used based on the round, bell and conical shapes [25]. The breasts were modelled as three-dimensional domains composed of skin, healthy tissue, and tumour, as shown in Fig. 1. The models have cup sizes in a range between B (5.08 cm) and C (7.62 cm), which are quite common worldwide [26]. The average skin thickness employed was of 1.5 mm [27]. Tumour depth (z) was established as the distance between the breast surface's tallest point and the tumour top point.

Table 1
Tissue layer properties.
Source: Adapted from [29,32].

Properties	Skin ($i = 1$)	Healthy tissue ($i = 2$)	Tumour ($i = 3$)
k (W/(m °C))	0.266	0.322	0.564
ρ (kg/m^3)	1110	1020	1020
c (J/(kg °C))	3060	3060	3060
$\omega_{i,bas}$ (1/s)	0.00222	0.00034	0.00598
$Q_{i,bas}$ (W/m^3)	0	450.0	65 400.0

Pennes bioheat equation, as described in Eq. (1), models heat transfer in living tissues by coupling heat conduction through tissue layers, heat convection between blood and tissue, and metabolic heat generation [28]. The equation was used to obtain the surface temperature profiles contained in the datasets.

$$\rho_i c_i \frac{\partial T_i}{\partial t} = k_i \nabla^2 T_i + \rho_b \omega_{b,i} c_{p,b} (T_b - T_i) + Q_i \tag{1}$$

where i represents the tissue layers, skin ($i = 1$), healthy tissue ($i = 2$), and tumour ($i = 3$). The ρ_i, c_i, T_i, k_i, ω_i, and Q_i are the specific mass, specific heat, temperature, thermal conductivity, blood perfusion rate and metabolic heat generation of each layer, respectively. The ρ_b, $c_{p,b}$, and T_b correspond to the blood's specific mass, specific heat, and temperature, with their values being 1060 kg/m^3, 3840 J/(kg °C), and 37 °C, respectively [29].

A tissue's metabolic heat generation and blood perfusion rate can vary due to the influence of local thermoregulation. Their values vary depending on the human body's need to maintain a constant core temperature due to thermal changes [30]. The metabolic heat generation and blood perfusion rate can be modelled by the van't Hoff effect [31], as shown in Eqs. (2) and (3).

$$Q_i(T) = Q_{i,bas} q_{i,10}^{\left(\frac{T-T_b}{10}\right)} \tag{2}$$

where $Q_{i,bas}$ represents the tissue's basal metabolic heat generation and $q_{i,10}$ is the metabolic heat coefficient.

$$\omega_{b,i}(T) = \omega_{i,bas} q_{b,10}^{\left(\frac{T-T_b}{10}\right)} \tag{3}$$

where $\omega_{i,bas}$ represents the tissue's basal blood perfusion rate and $q_{b,10}$ is the blood perfusion rate coefficient. The metabolic heat and blood perfusion coefficients have the same value, being equal to 1.1 in the tumour layer, representing a linear behaviour, and 2 in the other layers, representing an exponential behaviour [22,30,31]. The tissue layer's properties are shown in Table 1.

The types of boundary conditions used on the B1 breast model are shown in Fig. 2. The entire bottom layer was maintained at a constant body core temperature, as shown in Eq. (4), to describe the interface between a patient's thoracic wall and muscle layer. In passive thermography conditions, a convection boundary representing ambient natural convection was placed on the breast skin surface, as shown in Eq. (5). The same boundary configuration was used on breast models B2 and B3.

$$T_i(x, y, z, t)|_{bottom\ surface} = 37\ °\text{C},\ i = 1, 2 \tag{4}$$

$$-k_1 \left.\frac{\partial T_1}{\partial n}\right|_{top\ surface} = h\left(T_1(x, y, z, t)\big|_{top\ surface} - T_\infty\right) \tag{5}$$

where h is the heat convection coefficient and T_∞ is the ambient temperature, with their values being 13.5 W/(m^2 °C) and 21 °C, respectively [33].

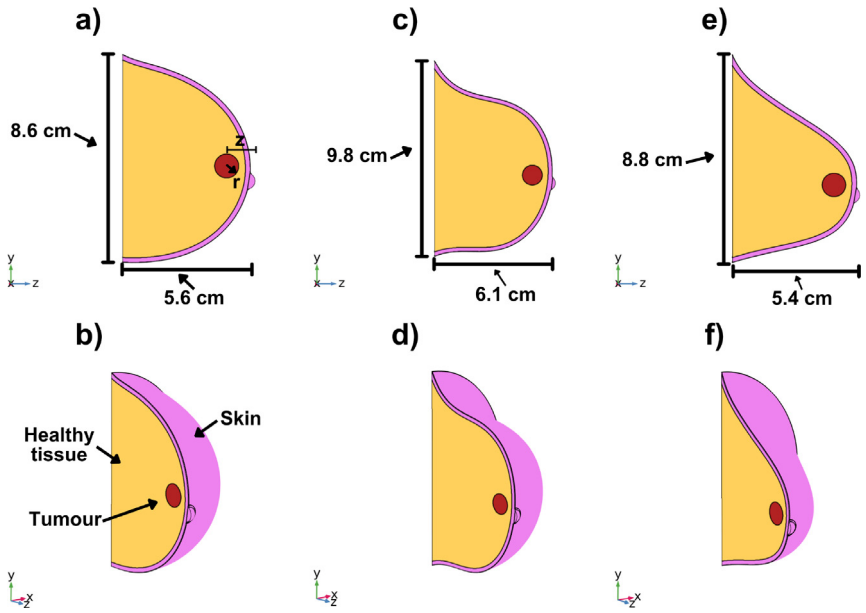


Fig. 1. Breast model's cross-section and 3-D view: (a, b) B1 model, (c, d) B2 model, and (e, f) B3 model.

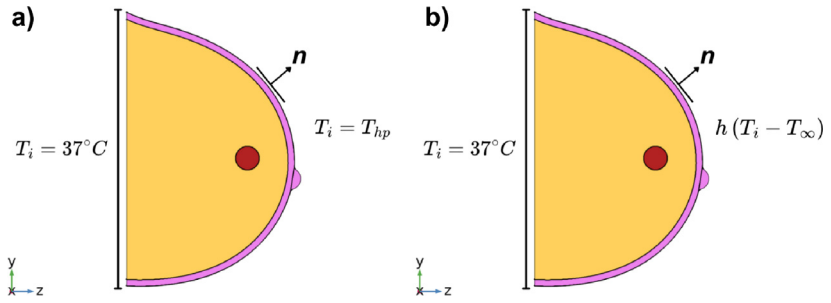


Fig. 2. Breast model B1 with (a) constant temperature boundary and (b) heat convection boundary.

In dynamic thermography conditions, the entire breast skin surface was maintained at a hypothermia temperature (T_{hp}) of 15 °C for 1800 s, describing the cold stress application. Afterwards, the boundary condition was switched to natural convection for 3600 s, as shown in Eqs. (6) and (7).

$$T_1(x,y,z,t)|_{top\ surface} = T_{hp},\ t \le 1800\ \text{s} \tag{6}$$

$$-k_1 \left.\frac{\partial T_1}{\partial n}\right|_{top\ surface} = h\left(T_1(x,y,z,t)\big|_{top\ surface} - T_\infty\right),\ 1800\ \text{s} < t \le 5400\ \text{s} \tag{7}$$

A 20 min at 15 °C cooling has been previously shown to enhance the thermal contrast of superficial and intermediate early-stage tumours [12]. Clinical studies have employed cooling temperatures below 10 °C, although for shorter periods [34,35]. Lower cooling temperatures can provide higher thermal contrasts, at the cost of increasing patient discomfort, with longer application periods providing smaller contrast improvements in comparison [17]. However, increasing the cooling time allows the use of higher hypothermia temperatures, causing less discomfort, but resulting in a more tiresome clinical exam.

The temperature and heat flux at the interface between tissue layers are described by Eqs. (8) and (9), respectively.

$$T_i(x,y,z,t)\big|_{interface} = T_{i+1}(x,y,z,t)\big|_{interface} \tag{8}$$

$$k_i \left.\frac{\partial T_i(x,y,z,t)}{\partial n}\right|_{interface} = k_{i+1} \left.\frac{\partial T_{i+1}(x,y,z,t)}{\partial n}\right|_{interface} \tag{9}$$

Thermal contrast, a parameter that measures the surface temperature difference between the same breast model with a tumour (cancerous) and without a tumour (healthy), was calculated by employing Eq. (10).

$$\Delta T = T_{cancerous} - T_{healthy} \tag{10}$$

where $T_{cancerous}$ is the surface temperature from the breast model with a tumour and $T_{healthy}$ is the surface temperature from the breast model without a tumour.

The mathematical model was solved using the commercial finite element software COMSOL Multiphysics®. A computational mesh with about 70 000 tetrahedral elements achieved convergence and was used to generate all of the studied cases.

2.2. Dataset generation

An algorithm in Java was developed in COMSOL Multiphysics Application Builder to change a tumour's size and location inside each breast model. One dataset was composed of three smaller datasets of 346 cases, one for each breast model, resulting in a total of 1038 solved cases. The datasets were generated for two different depth ranges, and the cases were solved for each type of thermography, resulting in four datasets. Spherical tumours with radii (r) of $0.375 \le r \le 0.50$ cm were generated inside the healthy tissue layer within different positions and

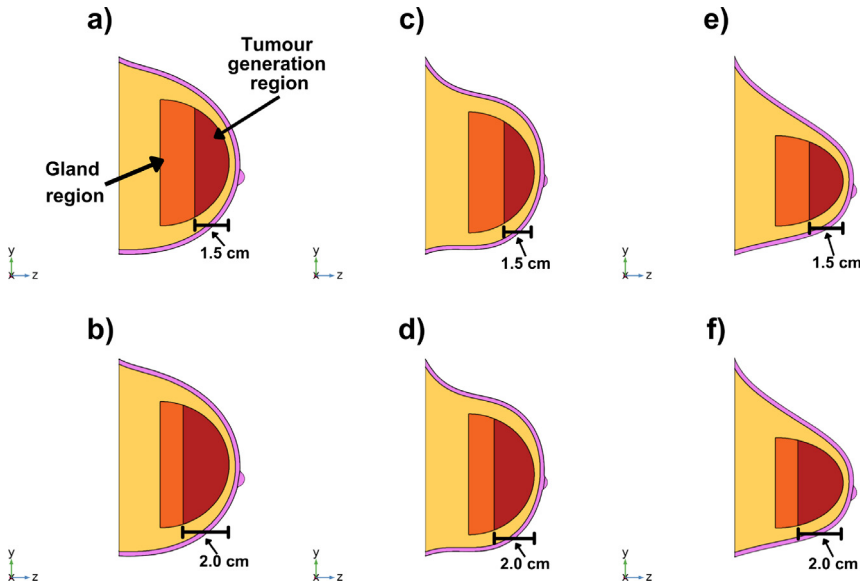


Fig. 3. Depth ranges DR1 and DR2: (a, b) B1 model, (c, d) B2 model, and (e, f) B3 model.

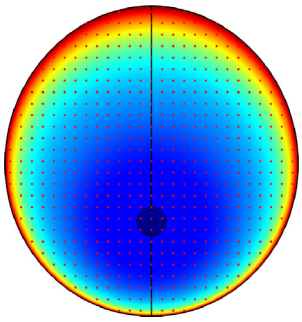


Fig. 4. Points on a surface temperature profile.

depth ranges. After placing a tumour, the breast model was solved and a new surface temperature profile was obtained. The temperature profiles corresponding to each depth range were arranged separately.

The generated tumours can be classified as (T1b, N0, M0), which is a type of stage 1 breast cancer that has no metastasis in the regional lymph nodes or distant regions. These tumours have sizes of $0.25 < r \leq 0.5$ cm, according to the TNM staging system [36]. At this stage, almost a 100% of the patients will survive for at least five years after the diagnosis, indicating the importance of detecting this type of tumour [37]. Fig. 3 shows the depth ranges of the tumours generated in each breast model. Tumours were generated following the trajectories between the upper and lower limit curves. The DR1 range consists of superficial tumours. In the DR2 range, deeper tumours were added to the dataset.

A total of 576 points were applied on the breast models surfaces to measure the skin temperatures more precisely, as shown in Fig. 4. These measurements were later used to generate 2-D temperature profiles. In dynamic thermography, the time step employed during the 60 min thermal recovery was 2 min, resulting in 31 temperature profiles. This time step provided the highest thermal contrasts and lower dataset generation times. In passive thermography, only one temperature profile was obtained. The steps performed to generate and arrange the datasets are shown in Fig. 5.

Principal Component Analysis (PCA) was used to compress the 2-D temperature data before training the neural network. PCA is a dimensionality reduction algorithm that provides a compact version of high dimensional data, such as images, based on the existing correlations between the dimensions, with the data varying significantly more in a certain dimension compared to the others [38].

Random noise was added to the simulated 2-D temperature profiles used to train the neural network, as described by Eq. (11), representing the measurement errors of an infrared camera.

$$T_{noisy} = T_{simulated} + \beta \tag{11}$$

where $T_{simulated}$ is the simulated temperature without noise and β is the random noise with an intensity of 2%, an error magnitude observed on infrared cameras [10,39,40]. The noise is relative to the simulated temperature measured in each point of a 2-D surface profile.

2.3. Neural network

Artificial neural networks are machine learning structures composed of neurons that simulate the learning mechanism in biological organisms. A neuron is a computational unit that contains weights (w_{ji}), biases (b_j), and an activation function (f), with the weights measuring the influence of the inputs on the neural network's estimates [41–43]. The mathematical representation of a neuron is described by Eq. (12).

$$y_j = f\left(\sum_{i=1}^{n} w_{ji}x_i + b_j\right) \tag{12}$$

where x_i is the input, i is input's number, n is the total number of inputs, and j is the node's number.

In a feedforward neural network, the neurons are layered, with the input and output layers being separated by intermediate (hidden) layers. This type of structure is used to learn parameters (weights and biases) and provide function approximations [42,43].

A feedforward neural network developed with PyTorch was used to estimate the breast tumour parameters. Its structure comprises one input layer with the same number of features provided by the dimensionality reduction process, three hidden layers with 24, 16, and 8 neurons, and an output layer with four outputs, one for each estimated parameter, as shown in Fig. 6.

A ReLU (Rectified Linear Unit) function, as described by Eq. (13), was employed in the three hidden layers. This activation function is used to incorporate non-linearity into a neural network and increase its modelling power. A linear function, as described by Eq. (14), was used on the output layer. It is often employed when the targeted output values are supposed to be real numbers [42].

$$f(x) = max\{x, 0\} \tag{13}$$

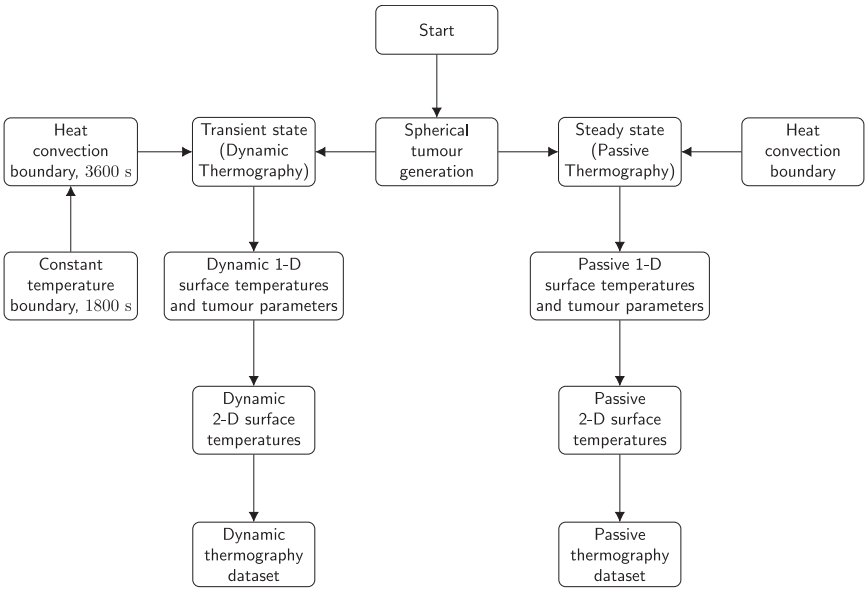


Fig. 5. Dataset generation flowgram.

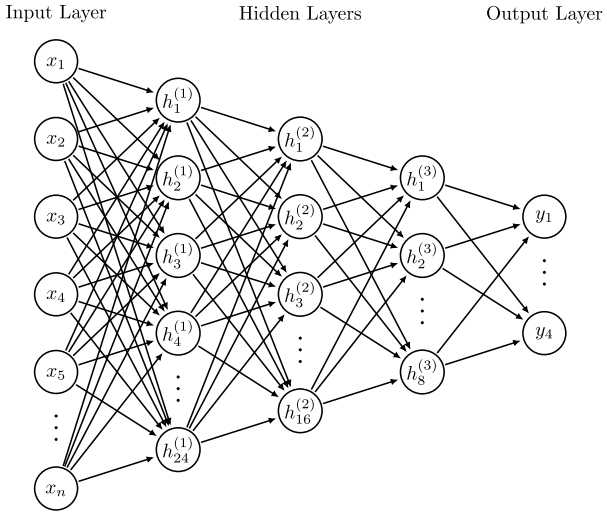


Fig. 6. Structure of the feedforward neural network.

$$f(x) = x \tag{14}$$

A mean square loss added to a L_2 norm, as described by Eq. (15), was used to compute the neural network's estimation errors. The sum's gradients are computed during training, and an optimization method updates the weights and biases. The optimizer focuses on minimizing the penalty term instead of the mean squared loss when the weights are too large. This approach is a type of regularization method commonly employed to prevent overfitting, when the model fits on the training data rather than the desired pattern [44].

$$L = \frac{1}{N}\sum_{i=1}^{N}(y_i^{est} - y_i^{tar})^2 + \lambda\|w\|^2 \tag{15}$$

where N is the number of samples, y_i^{est} is the estimated value, y_i^{tar} is the targeted value, and λ is the regularization constant.

The data was divided into 50% for training, 25% for validation, and 25% for testing. The learning rate and regularization coefficient employed were 1×10^{-5} and 1×10^{-3}, with this combination providing the lowest validation loss for dynamic thermography and the third lowest for passive thermography, with dynamic thermography also showing a loss decrease in this scenario, as shown in Fig. 7. Weights and biases were updated using the Adam optimizer for 10 000 epochs, enough training for the neural network to reach convergence, as shown in Fig. 8. The calculations were made in a laptop with a Intel i7 - 12700H processor, a RTX 3050 4 GB graphics card, and 16 GB of DDR4 RAM, with a runtime of 54.965 min. The input data was scaled between a −1, 1 range and standardized before the dimensionality reduction process. It was specified that PCA would compress the temperature data while retaining features that add up to 95% of each dataset's variance, as shown in Fig. 9. The training and testing processes of the neural network were repeated 11 times, resulting in 11 396 estimates, 2849 for each parameter. Afterwards, the mean relative errors and standard deviations of x, y, z, and r were calculated.

3. Results and discussion

3.1. Estimating tumour parameters

Fig. 10 shows the mean relative error of each DR1 tumour parameter using passive and dynamic thermography. Tumours x and y coordinates had the lowest and closest errors due to causing the most similar and most significant temperature variations on the skin surface, showing mean estimation errors close to 3% and 2% when using passive and dynamic thermography, respectively. Tumour radius and depth similarly alter the surface temperature profiles, influencing the size and magnitude of the tumour's thermal response, but in different intensities, with smaller and deeper tumours having the lowest thermal contrasts. The depth and radius estimation errors were close to 6% and 9% using passive thermography, as well as 4% and 6% using dynamic thermography. The mean estimation errors were up to 33.25% lower for dynamic thermography.

Fig. 11 shows the estimation error histogram for DR1 tumour parameters with a 2% noise using passive and dynamic thermography. The estimated tumour parameters showed high standard deviations. However, using passive thermography, about 84.99% of the estimates had relative errors lower or equal than 10%. In this case, the neural network makes accurate estimates, but has a chance of failure, showing a maximum error of 39.54%. Using dynamic thermography, about 92.26% of the estimates had relative errors lower or equal to 10%, with a maximum error of 24.44%. Thus, dynamic thermography provides a

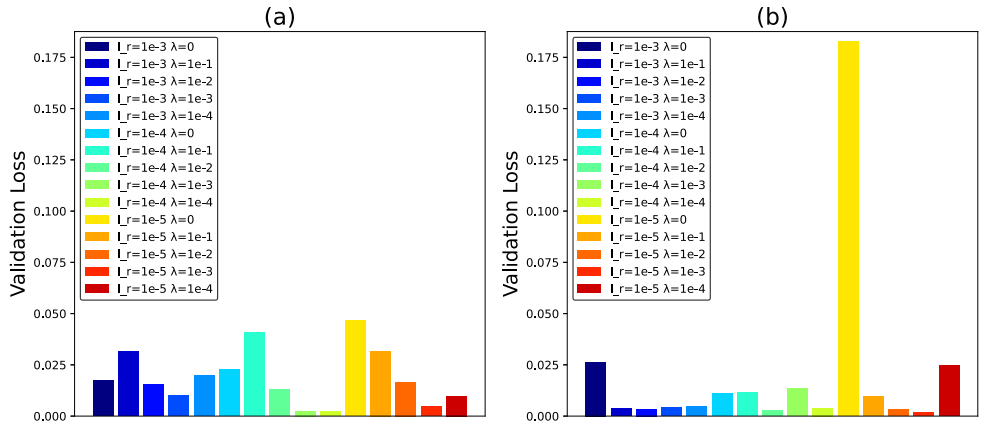


Fig. 7. Validation loss at the end of training for DR1 dataset: (a) passive and (b) dynamic thermography.

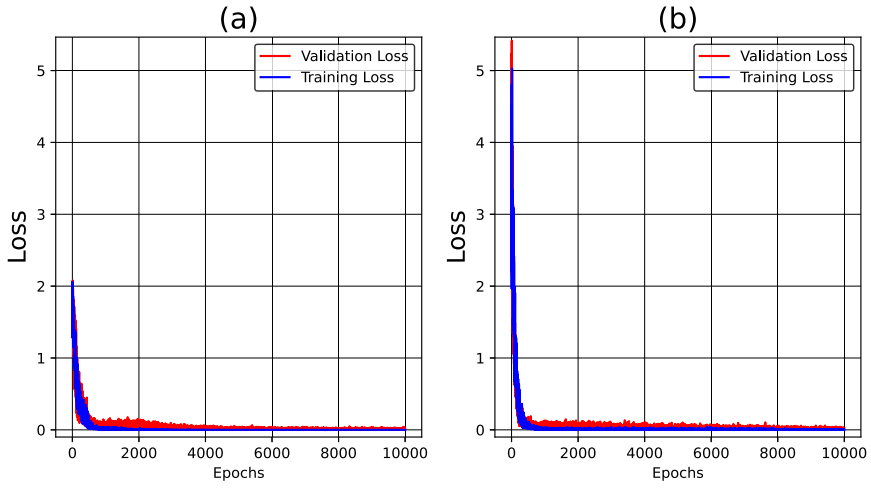


Fig. 8. Loss convergence for DR1 dataset: (a) passive and (b) dynamic thermography.

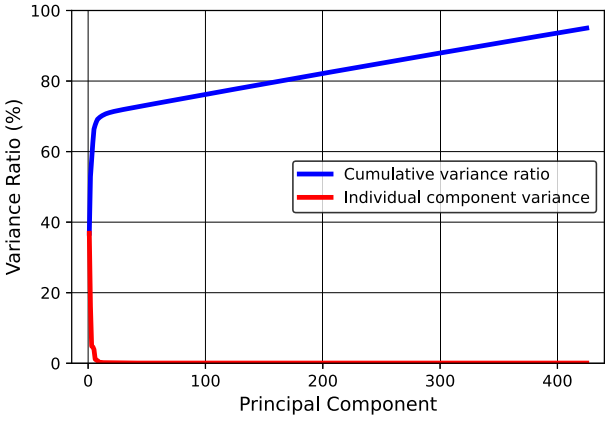


Fig. 9. PCA variance ratio for DR1 dynamic thermography dataset.

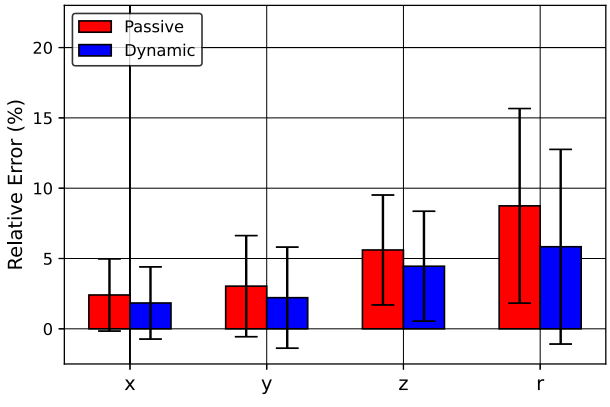


Fig. 10. DR1 tumour parameters mean relative error and standard deviation.

higher estimation accuracy.

Fig. 12 shows the maximum and minimum thermal contrasts of DR1 tumours without noise for both types of thermography. Dynamic thermography had surface temperature variations more than 150% higher than passive thermography, making the temperature profiles less noise-sensitive, benefiting smaller and deeper tumours that generate low thermal responses, improving the neural network's estimation accuracy. In this study, the noise magnitude reached close to 0.7 °C, which is about 216% higher than the minimum thermal contrast in passive thermography and 24% in dynamic thermography. Many cases passed the parameters noise thresholds, were the patterns become unrecognizable, contributing to the amount of inaccurate estimates encountered, with dynamic thermography being less affected due to higher temperature variations.

Fig. 13 shows the mean relative error of each DR2 tumour parameter using passive and dynamic thermography. Coordinates x and y showed mean estimation errors close to 4% and 3% when using passive

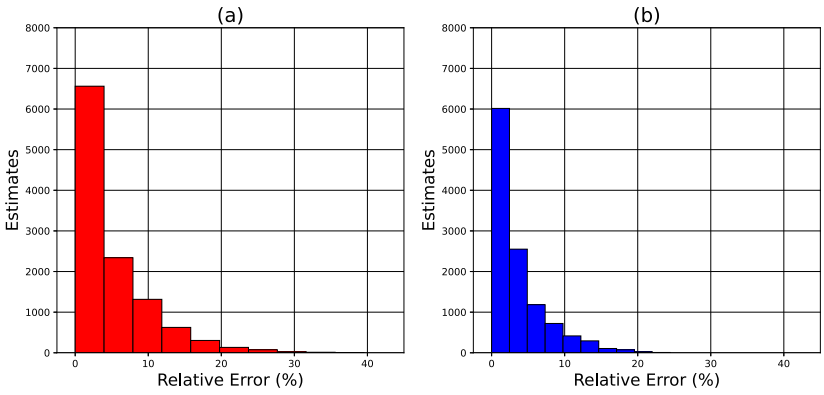


Fig. 11. Estimation error histogram for DR1 tumour parameters: (a) passive and (b) dynamic thermography.

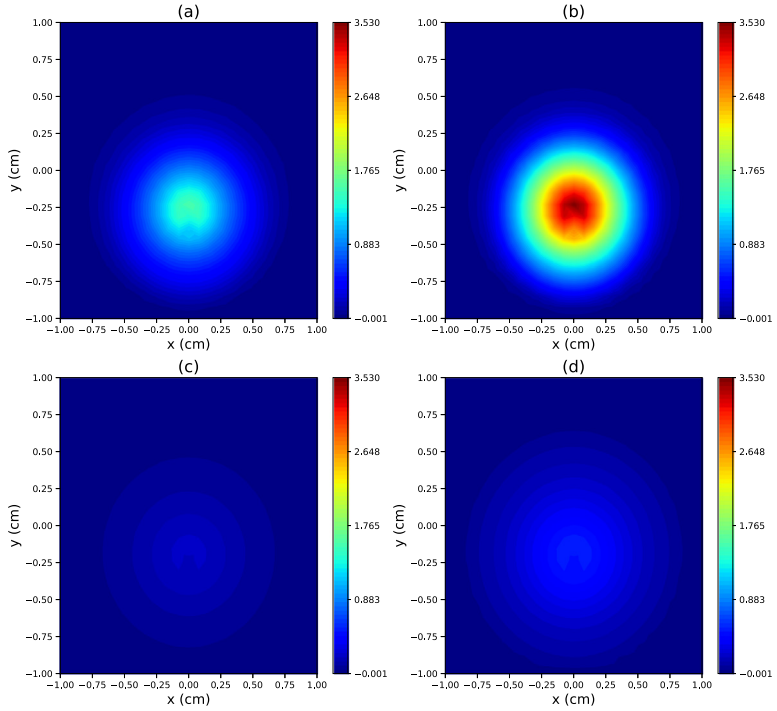


Fig. 12. DR1 tumours maximum and minimum thermal contrast: (a, c) passive and (b, d) dynamic thermography.

and dynamic thermography, respectively. The depth and radius estimation errors were close to 6% and 12% using passive thermography, as well as 5% and 8% using dynamic thermography. The mean estimation errors were up to 29.70% lower for dynamic thermography. Adding deeper tumours to the datasets caused mean error increases of up to 43.64% and 51.27% when using passive and dynamic thermography, respectively.

Fig. 14 shows the estimation error histogram for DR2 tumour parameters with a 2% noise using passive and dynamic thermography. Using passive thermography, about 77.94% of the estimates had relative errors lower or equal than 10%. In this case, the neural network makes accurate estimates, but has a chance of failure, showing a maximum error of 51.77%. Using dynamic thermography, about 86.2% of the estimates had relative errors lower or equal to 10%, with a maximum error of 38.30%. Adding deeper tumours reduced the neural network's estimation accuracy.

Fig. 15 shows the maximum and minimum thermal contrasts of DR2 tumours without noise for both types of thermography. Dynamic thermography had surface temperature variations more than 150% higher than passive thermography, improving the neural network's estimation accuracy. A noise magnitude of 0.7 °C is more than 480%

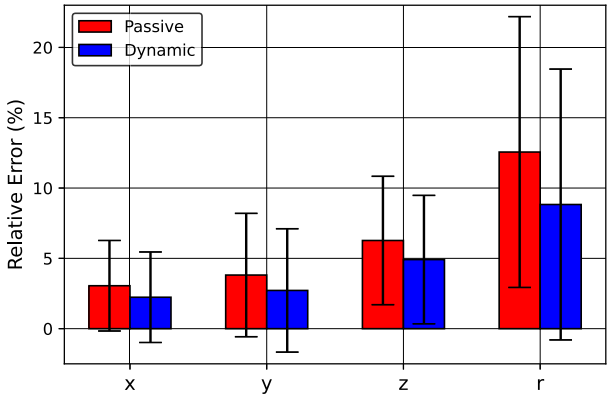


Fig. 13. DR2 tumour parameters mean relative error and standard deviation.

higher than the minimum thermal contrast in passive thermography and 130% in dynamic thermography. This means that even more cases passed the parameters noise thresholds compared to the previous depth

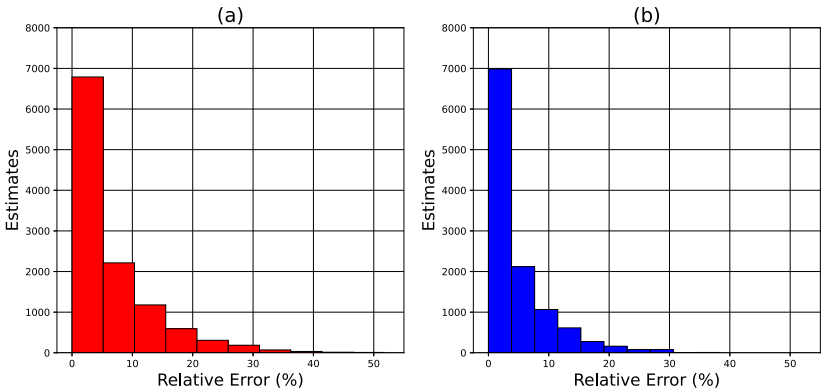


Fig. 14. Estimation error histogram for DR2 tumour parameters: (a) passive and (b) dynamic thermography.

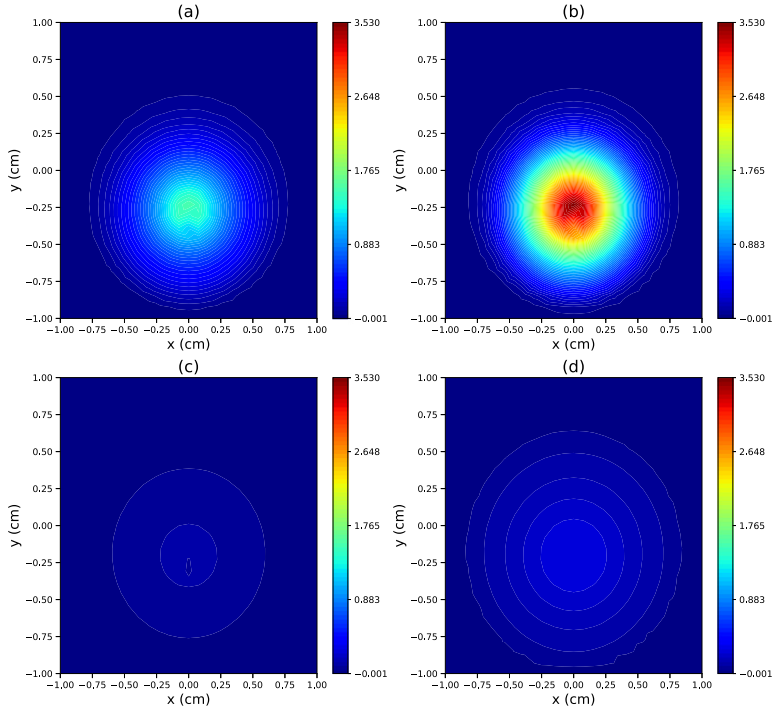


Fig. 15. DR2 tumours maximum and minimum thermal contrast: (a, c) passive and (b, d) dynamic thermography.

range, increasing the amount of inaccurate estimates and their errors in both types of thermography.

3.2. Influence of thermal contrast

Fig. 16 shows the normalized thermal contrast variation caused by x and y of two different cases and under various noise intensities. The thermal pattern's position on the skin surface is determined by tumour's coordinates x and y, with its shape being influenced by the breast's geometry, which establishes how the heat will be distributed on the surface. The pattern's centre can be located on the surface without much difficulty with a 50% noise in both cases. For a 100% noise, the task is harder, with some temperature maps across the surface reaching a close value to the thermal signal's centre, but it is still possible, with the highest thermal contrast region remaining visible. This indicates that the tumour's coordinates x and y can be accurately estimated even with noise magnitudes that approach the maximum thermal contrast, being the reason why these parameters showed the lowest mean estimation errors.

Fig. 17 shows the normalized thermal contrast variation caused by z of two different cases and under various noise intensities. The heat generated by a shallow tumour has less space to propagate, so it concentrates on a smaller region, forming a smaller thermal pattern with a higher contrast on the surface. After adding a 50% noise, the thermal signal was distorted, being difficult to identify its size and shape in both cases. However, there was a significant contrast difference between case 1 and case 2, being possible to distinguish one from the other. For a 100% noise, its much harder to recognize the patterns due to the various temperature maps across the surface. This indicates that the tumour's depth can be accurately estimated with noise magnitudes that are close to 50% of the maximum thermal contrast.

Fig. 18 shows the normalized thermal contrast variation caused by r of two different cases and under various noise intensities. Larger tumours generate more heat and have more surface area compared to smaller ones, resulting in bigger thermal patterns and higher thermal contrasts. For a 50% noise, the thermal signal was distorted, being very difficult to identify its size and shape, and to distinguish each case. Increasing the noise to 100% noise only made the task harder. This indicates that r can only be accurately estimated with noise intensities significantly lower than 50% of the maximum thermal contrast. Its noise sensitivity was associated with the high mean estimation errors encountered.

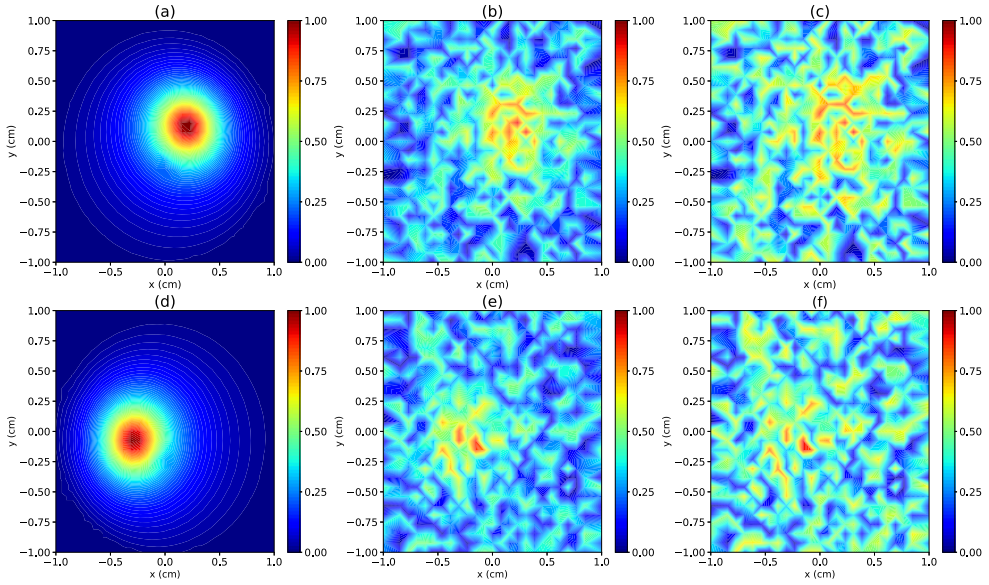


Fig. 16. Normalized thermal contrast variation of x and y: (a) Case 1, (b) Case 1 with 50% noise, (c) Case 1 with 100% noise, (d) Case 2, (e) Case 2 with 50% noise, and (f) Case 2 with 100% noise.

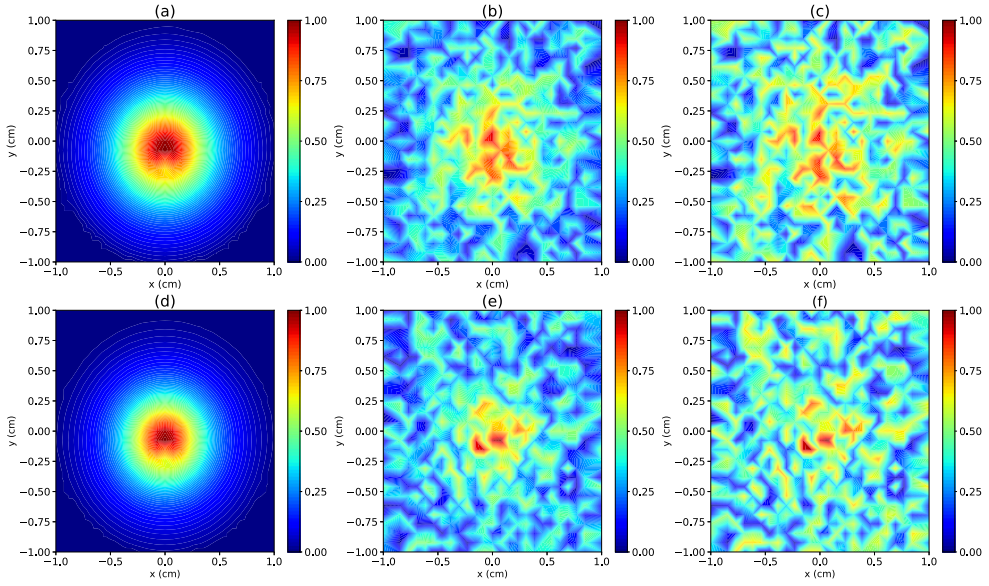


Fig. 17. Normalized thermal contrast variation of z: (a) Case 1, (b) Case 1 with 50% noise, (c) Case 1 with 100% noise, (d) Case 2, (e) Case 2 with 50% noise, and (f) Case 2 with 100% noise.

Fig. 19 shows DR1 tumours estimation errors of x, y, z and r using dynamic thermography. In about 24% of the cases, the noise magnitude of 0.7 °C was equal to or above 50% of the thermal contrast. It was previously seen that coordinates x and y noise thresholds are close to 100% of the thermal contrast, and z and r thresholds are close to and below 50%, respectively, with the parameters that had the lowest thresholds showing the largest amount of inaccurate estimates. The radius had about 20.4% of its estimates with errors above 10%, also being responsible for the highest errors of the dataset, indicating that this parameter can only be accurately predicted for shallower and larger tumours, due to its low noise threshold. For small and deep tumours, the hypothermia conditions capable of providing the necessary thermal contrast for this parameter might be too aggressive, prohibiting its practical use due to patient's discomfort.

Tumour depth has also shown to be more noise sensitive, with 7% of its estimates errors being higher than 10%, although using a more aggressive cold stress has the potential to reduce these inaccuracies, with the hypothermia conditions being more acceptable due to its higher noise threshold. About 0.95% and 2.6% of the estimates of coordinates x and y had errors higher than 10%, with both parameters having the highest noise thresholds. The results also showed that temperature profiles with a high thermal contrast can have higher estimation errors than lower thermal contrast ones in the same dataset. A total of 92.26% of the estimates had relative errors below 10%, and only 37% were cases with more than 2 °C of thermal contrast in the testing set.

4. Conclusion

This work used a feedforward neural network developed in Pytorch to estimate the size and location of early-stage breast tumours based on surface temperature data. Three breast models with thermoregulation were solved numerically using the commercial software COMSOL Multiphysics® under passive and dynamic thermography conditions.

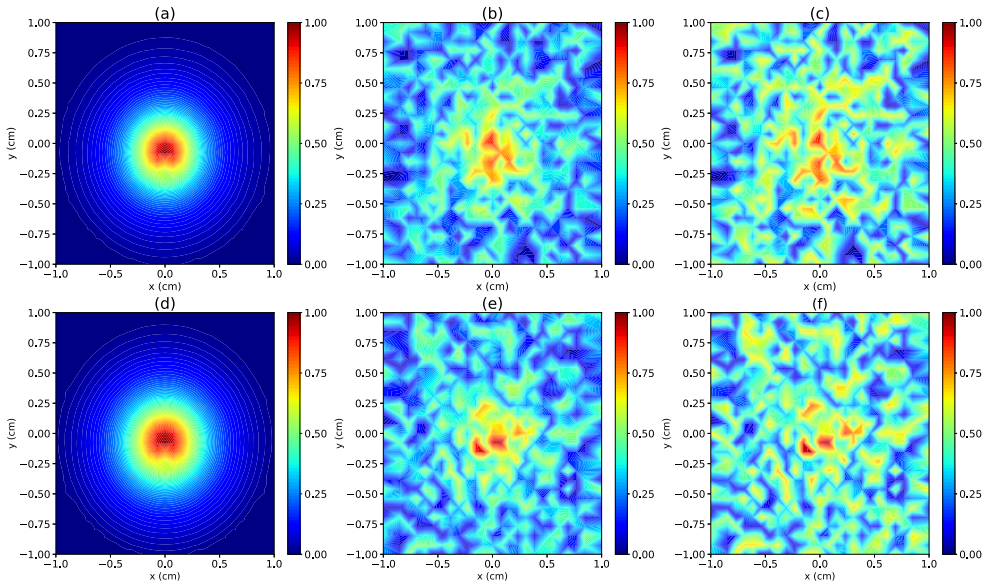


Fig. 18. Normalized thermal contrast variation of *r*: (a) Case 1, (b) Case 1 with 50% noise, (c) Case 1 with 100% noise, (d) Case 2, (e) Case 2 with 50% noise, and (f) Case 2 with 100% noise.

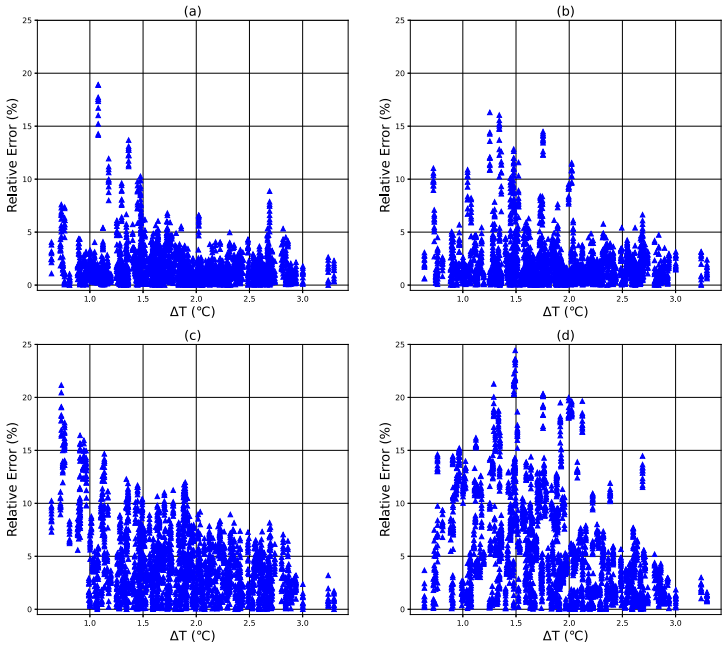


Fig. 19. DR1 tumour estimation errors using dynamic thermography: (a) *x*, (b) *y*, (c) *z*, and (d) *r*.

The dynamic thermography procedure was based on applying hypothermia and thermal recovery at specific times. Various datasets composed of surface temperature data were generated and used to train the neural network. The estimates in two different depth ranges were investigated.

The neural network's estimation accuracy significantly improved with dynamic thermography, reducing mean errors by up to 33.25% for DR1 tumours and 29.70% for DR2 tumours. This was associated with higher surface temperature variations, which improves the thermal response of smaller and deeper tumours. Adding deeper tumours to a dataset reduced the neural network's estimation accuracy, with the individual thermal contrast of a surface temperature profile not determining its estimation error.

The relation between thermal contrast and noise threshold directly influenced the estimates, with the parameters with the lowest noise thresholds providing the highest errors. Lower cooling temperatures and longer application periods should be used to increase the thermal contrast of smaller and deeper tumours, and reduce the errors. However, the necessary hypothermia conditions for properly estimating the radius might be too aggressive for small deep tumours, restricting its estimation for larger shallow tumours.

The main contribution of this work was to show the limits of using each type of thermography and provide information that could help improve the accuracy of estimating the size and location of early-stage breast tumours using surface temperature data and a neural network. In further work, different combinations of cooling temperatures and application periods should be tested and compared to find an optimal value between estimation accuracy and patient discomfort. Furthermore, the influence of thermal contrast and noise thresholds for breast cancer diagnosis and patient-specific tumour parameter estimation should be

investigated. Finally, real dynamic thermographic image acquisition and estimation of breast tumour cases with the algorithm developed will be performed.

CRediT authorship contribution statement

M.F.B. Moraes: Conceptualization, Methodology, Software, Validation, Writing - Original Draft. **S. Sfarra:** Formal analysis, Writing - Review & Editing, Supervision. **H. Fernandes:** Validation, Writing - Review & Editing. **A.A.A. Figueiredo:** Conceptualization, Methodology, Software, Validation, Writing - Review & Editing, Supervision.

Declaration of competing interest

The authors declare that they have no known competing financial interests or personal relationships that could have appeared to influence the work reported in this paper.

Acknowledgements

This study was financed in part by the Coordenação de Aperfeiçoamento de Pessoal de Nível Superior - Brazil (CAPES) - Finance Code 001. H.F. is grateful for the support provided by the Conselho Nacional de Desenvolvimento Científico e Tecnológico - Brazil (CNPq) - Finance Code 312530/2023-4.

Data availability

Data will be made available on request.

References

[1] Cancer today, 2024, https://gco.iarc.fr/today/en, (Accessed 03 May 2024).
[2] L. Balkenende, J. Teuwen, R.M. Mann, Application of deep learning in breast cancer imaging, in: Seminars in Nuclear Medicine, Vol. 52, Elsevier, 2022, pp. 584–596, http://dx.doi.org/10.1053/j.semnuclmed.2022.02.003.
[3] H. Blumen, K. Fitch, V. Polkus, Comparison of treatment costs for breast cancer, by tumor stage and type of service, Am. Heal. Drug Benefits 9 (1) (2016) 23.
[4] S.H. Jafari, Z. Saadatpour, A. Salmaninejad, F. Momeni, M. Mokhtari, J.S. Nahand, M. Rahmati, H. Mirzaei, M. Kianmehr, Breast cancer diagnosis: Imaging techniques and biochemical markers, J. Cell. Physiol. 233 (7) (2018) 5200–5213, http://dx.doi.org/10.1002/jcp.26379.
[5] A.A. Figueiredo, H.C. Fernandes, F.C. Malheiros, G. Guimaraes, Influence analysis of thermophysical properties on temperature profiles on the breast skin surface, Int. Commun. Heat Mass Transfer 111 (2020) 104453, http://dx.doi.org/10.1016/j.icheatmasstransfer.2019.104453.
[6] N.F. Boyd, H. Guo, L.J. Martin, L. Sun, J. Stone, E. Fishell, R.A. Jong, G. Hislop, A. Chiarelli, S. Minkin, et al., Mammographic density and the risk and detection of breast cancer, N. Engl. J. Med. 356 (3) (2007) 227–236, http://dx.doi.org/10.1056/NEJMoa062790.
[7] A. Amri, S.H. Pulko, A.J. Wilkinson, Potentialities of steady-state and transient thermography in breast tumour depth detection: A numerical study, Comput. Methods Programs Biomed. 123 (2016) 68–80, http://dx.doi.org/10.1016/j.cmpb.2015.09.014.
[8] R. Hatwar, C. Herman, Inverse method for quantitative characterisation of breast tumours from surface temperature data, Int. J. Hyperth. 33 (7) (2017) 741–757, http://dx.doi.org/10.1080/02656736.2017.1306758.
[9] J.-L. Gonzalez-Hernandez, A.N. Recinella, S.G. Kandlikar, D. Dabydeen, L. Medeiros, P. Phatak, Technology, application and potential of dynamic breast thermography for the detection of breast cancer, Int. J. Heat Mass Transfer 131 (2019) 558–573, http://dx.doi.org/10.1016/j.ijheatmasstransfer.2018.11.089.
[10] A. Mashekova, Y. Zhao, E.Y. Ng, V. Zarikas, S.C. Fok, O. Mukhmetov, Early detection of the breast cancer using infrared technology–a comprehensive review, Therm. Sci. Eng. Prog. 27 (2022) 101142, http://dx.doi.org/10.1016/j.tsep.2021.101142.
[11] T. Gomboc, J. Iljaž, L. Wrobel, M. Hriberšek, J. Marn, Design of constant temperature cooling device for melanoma screening by dynamic thermography, Eng. Anal. Bound. Elem. 125 (2021) 66–79, http://dx.doi.org/10.1016/j.enganabound.2021.01.009.
[12] T.C. Barros, A.A.A. Figueiredo, Three-dimensional numerical evaluation of skin surface thermal contrast by application of hypothermia at different depths and sizes of the breast tumor, Comput. Methods Programs Biomed. 236 (2023) 107562, http://dx.doi.org/10.1016/j.cmpb.2023.107562.
[13] V. Mishra, S.K. Rath, D.P. Mohapatra, Thermograms-based detection of cancerous tumors in breasts applying texture features, Quant. InfraRed Thermogr. J. (2023) 1–26, http://dx.doi.org/10.1080/17686733.2023.2174341.
[14] J. Verstockt, R. Somers, F. Thiessen, I. Hoorens, L. Brochez, G. Steenackers, Finite element skin models as additional data for dynamic infrared thermography on skin lesions, Quant. InfraRed Thermogr. J. (2023) 1–20, http://dx.doi.org/10.1080/17686733.2023.2256998.
[15] Z.-S. Deng, J. Liu, Enhancement of thermal diagnostics on tumors underneath the skin by induced evaporation, in: 2005 IEEE Engineering in Medicine and Biology 27th Annual Conference, IEEE, 2006, pp. 7525–7528, http://dx.doi.org/10.1109/IEMBS.2005.1616253.
[16] T.-Y. Cheng, C. Herman, Analysis of skin cooling for quantitative dynamic infrared imaging of near-surface lesions, Int. J. Therm. Sci. 86 (2014) 175–188, http://dx.doi.org/10.1016/j.ijthermalsci.2014.06.033.
[17] Y. Zhou, C. Herman, Optimization of skin cooling by computational modeling for early thermographic detection of breast cancer, Int. J. Heat Mass Transfer 126 (2018) 864–876, http://dx.doi.org/10.1016/j.ijheatmasstransfer.2018.05.129.
[18] G. Jacob, I. Jose, S. Sujatha, Breast cancer detection: A comparative review on passive and active thermography, Infrared Phys. Technol. (2023) 104932, http://dx.doi.org/10.1016/j.infrared.2023.104932.
[19] S. Mitra, C. Balaji, A neural network based estimation of tumour parameters from a breast thermogram, Int. J. Heat Mass Transfer 53 (21–22) (2010) 4714–4727, http://dx.doi.org/10.1016/j.ijheatmasstransfer.2010.06.020.
[20] E. Saniei, S. Setayeshi, M.E. Akbari, M. Navid, Parameter estimation of breast tumour using dynamic neural network from thermal pattern, J. Adv. Res. 7 (6) (2016) 1045–1055, http://dx.doi.org/10.1016/j.jare.2016.05.005.
[21] J. Majdoubi, A.S. Iyer, A.M. Ashique, D.A. Perumal, Y. Mahrous, M. Rahimi-Gorji, A. Issakhov, Estimation of tumor parameters using neural networks for inverse bioheat problem, Comput. Methods Programs Biomed. 205 (2021) 106092, http://dx.doi.org/10.1016/j.cmpb.2021.106092.
[22] H. Chen, K. Wang, Z. Liu, H. Zhou, Surface temperature analysis and thermophysical property estimation for breast cancer by deep learning, Numer. Heat Transf. Part A: Appl. 82 (8) (2022) 411–427, http://dx.doi.org/10.1080/10407782.2022.2079298.
[23] Z. Khomsi, M. El Fezazi, L. Bellarbi, CNN-based approach for non-invasive estimation of breast tumor size and location using thermographic images, Int. J. Online Biomed. Eng. 20 (4) (2024) http://dx.doi.org/10.3991/ijoe.v20i04.46387.
[24] J. Eske, Breast shapes: What to know — medicalnewstoday.com, 2020, https://www.medicalnewstoday.com/articles/breast-shapes, (Accessed 25 October 2024).
[25] M. Johnson, 10 things to know about your breast size, 2023, URL https://www.healthline.com/health/average-breast-size.
[26] W.P. Review, Breast size by country 2024, 2024, URL https://worldpopulationreview.com/country-rankings/breast-size-by-country.
[27] L. Shi, S. Vedantham, A. Karellas, A.M. O'Connell, Skin thickness measurements using high-resolution flat-panel cone-beam dedicated breast CT a, Med. Phys. 40 (3) (2013) 031913, http://dx.doi.org/10.1118/1.4793257.
[28] H.H. Pennes, Analysis of tissue and arterial blood temperatures in the resting human forearm, J. Appl. Physiol. 1 (2) (1948) 93–122, http://dx.doi.org/10.1152/jappl.1998.85.1.5.
[29] J.-L. Gonzalez-Hernandez, A.N. Recinella, S.G. Kandlikar, D. Dabydeen, L. Medeiros, P. Phatak, An inverse heat transfer approach for patient-specific breast cancer detection and tumor localization using surface thermal images in the prone position, Infrared Phys. Technol. 105 (2020) 103202, http://dx.doi.org/10.1016/j.infrared.2020.103202.
[30] J. Iljaž, L.C. Wrobel, M. Hriberšek, J. Marn, Numerical modelling of skin tumour tissue with temperature-dependent properties for dynamic thermography, Comput. Biol. Med. 112 (2019) 103367, http://dx.doi.org/10.1016/j.compbiomed.2019.103367.
[31] H. Chen, K. Wang, Z. Du, W. Liu, Z. Liu, Predicting the thermophysical properties of skin tumor based on the surface temperature and deep learning, Int. J. Heat Mass Transfer 180 (2021) 121804, http://dx.doi.org/10.1016/j.ijheatmasstransfer.2021.121804.
[32] A. Lozano III, J.C. Hayes, L.M. Compton, J. Azarnoosh, F. Hassanipour, Determining the thermal characteristics of breast cancer based on high-resolution infrared imaging, 3D breast scans, and magnetic resonance imaging, Sci. Rep. 10 (1) (2020) 10105, http://dx.doi.org/10.1038/s41598-020-66926-6.
[33] C. Gutierrez, A. Owens, L. Medeiros, D. Dabydeen, N. Sritharan, P. Phatak, S.G. Kandlikar, Breast cancer detection using enhanced IRI-numerical engine and inverse heat transfer modeling: model description and clinical validation, Sci. Rep. 14 (1) (2024) 3316, http://dx.doi.org/10.1038/s41598-024-53856-w.
[34] E. Lääperi, Cold provocation improves breast cancer detection with IR thermography: a pilot study, 2014.
[35] T. Sarigoz, T. Ertan, Role of dynamic thermography in diagnosis of nodal involvement in patients with breast cancer: A pilot study, Infrared Phys. Technol. 108 (2020) 103336, http://dx.doi.org/10.1016/j.infrared.2020.103336.
[36] L.H. Sobin, M.K. Gospodarowicz, C. Wittekind, TNM Classification of Malignant Tumours, John Wiley & Sons, 2011.
[37] Survival for breast cancer, 2023, https://www.cancerresearchuk.org/about-cancer/breast-cancer/survival, (Accessed 16 February 2024).

[38] M.P. Deisenroth, A.A. Faisal, C.S. Ong, Mathematics for Machine Learning, Cambridge University Press, 2020, http://dx.doi.org/10.1017/9781108679930.
[39] A. Morales-Cervantes, E.S. Kolosovas-Machuca, E. Guevara, M.M. Reducindo, A.B.B. Hernández, M.R. García, F.J. González, An automated method for the evaluation of breast cancer using infrared thermography, EXCLI J. 17 (2018) 989, http://dx.doi.org/10.17179/excli2018-1735.
[40] G. D'Alessandro, P. Tavakolian, S. Sfarra, A review of techniques and bio-heat transfer models supporting infrared thermal imaging for diagnosis of malignancy, Appl. Sci. 14 (4) (2024) 1603, http://dx.doi.org/10.3390/app14041603.
[41] S. Haykin, Neural Networks and Learning Machines, 3/E, Pearson Education India, 2009.
[42] C.C. Aggarwal, et al., Neural networks and deep learning, Springer 10 (978) (2018) 3, http://dx.doi.org/10.1007/978-3-031-29642-0.
[43] I. Goodfellow, Y. Bengio, A. Courville, Deep Learning, MIT Press, 2016.
[44] A. Zhang, Z.C. Lipton, M. Li, A.J. Smola, Dive into Deep Learning, Cambridge University Press, 2023.



https://dspace.org/

Influence of thermal contrast and limitations of a deep-learning based estimation of early-stage tumour parameters in different breast shapes using simulated passive and dynamic thermography

Moraes, Mateus Felipe Benicio; Sfarra, Stefano; Fernandes, Henrique; Figueiredo, Alisson A. A.

2025-04
Elsevier
https://doi.org/10.1016/j.tsep.2025.103418
Moraes MFB, Sfarra S, Fernandes H, Figueiredo AAA. (2025) Influence of thermal contrast and limitations of a deep-learning based estimation of early-stage tumour parameters in different breast shapes using simulated passive and dynamic thermography. Thermal Science and Engineering Progress, Volume 60, April 2025, Article number 103418

Downloaded from a DSpace repository. https://dspace.org/